

## Design of Highly Stable and Efficient Bifunctional MXene-Based Electrocatalysts for Oxygen Reduction and Evolution Reactions

Xinwei Yang,<sup>1,2,3</sup> Xilin Zhang,<sup>1</sup> Zhansheng Lu,<sup>1</sup> Zongxian Yang<sup>1,\*</sup> and Ruqian Wu<sup>4,†</sup>

<sup>1</sup> School of Physics, Henan Normal University, Xinxiang, Henan 453007 China

<sup>2</sup> College of Electronic and Electrical Engineering, Henan Normal University, Xinxiang, Henan 453007, China

<sup>3</sup> Henan Key Laboratory of Optoelectronic Sensing Integrated Application, Xinxiang, Henan 453007, China

<sup>4</sup> Department of Physics and Astronomy, University of California, Irvine, California 92697-4575, USA



(Received 9 September 2020; revised 18 January 2021; accepted 18 March 2021; published 30 April 2021)

Finding low-cost, highly active, and thermally stable bifunctional electrocatalysts toward oxygen reduction and evolution reactions (ORR-OER) is a key for the development of renewable energy devices, including fuel cells and water splitting. Here, we systematically investigate the physical properties, structural stability, and ORR-OER bifunctional catalytic activity of Pt supported by a series of *MXene* substrates using density-functional-theory calculations. Our results indicate that Pt atoms disperse uniformly on the *MXene* supports with high structural stability at high temperature and oxidation conditions, because of the strong metal-support interaction. The lattice parameter of *MXenes* is found to play a crucial role in determining the morphology and stability of these heterostructures and a descriptor is proposed for their design. In particular, Pt/V<sub>2</sub>C is identified as the stable and most promising bifunctional catalyst with an overpotential comparable to the benchmarks. This work brings up a strategy for the search and design of superb transition metal/*MXene* catalysts for energy applications.

DOI: 10.1103/PhysRevApplied.15.044053

### I. INTRODUCTION

Proton-exchange membrane fuel cells (PEMFCs), being developed mainly for vehicle and other mobile applications, are recognized as a prime candidate to solve the energy crisis and environmental issues [1]. To date, almost all current PEMFCs use a Pt/C catalyst (Pt particles on carbon) to catalyze the reactions on the electrode, in which carbon acts as an electrical conductor and Pt particles are the catalyst. However, the high cost, poor stability, and low activity of the Pt/C catalyst in the cathode oxygen reduction reaction (ORR) inhibit the commercialization of PEMFCs. Particularly, the weak interaction between Pt NPs and carbon support results in aggregation of Pt and a decrease in the electrochemical surface area (ECSA) of Pt with long-term operation [2–5]. Wei and co-workers [6] found that the Pt/C catalyst lost approximately 48% ECSA after 1500 cycles. Besides, the carbon support is vulnerable to be corroded in reaction conditions, leading to the separation of Pt from the support, which is a major reason for the degradation of catalytic activity and stability of the Pt/C cathode.

To reduce the use of precious metals and also to prevent their degradation in reaction conditions, catalysts with

strong metal-support interaction (SMSI) appear to be very promising [7,8]. With appropriate material combinations, SMSI may force metal atoms to uniformly disperse on substrates with high structural stability, and also allows tuning their electronic properties in a large range for achieving enhanced catalytic activity. However, the search of such excellent combinations with ideal chemical and physical characteristics and desired catalytic performance remains a huge challenge [9,10]. With high metallicity and unique morphologies [11–15], two-dimensional transition metal carbides (*MXenes*, with a formula of M<sub>n+1</sub>C<sub>n</sub>T<sub>x</sub>) have been identified as promising supports and prominent conducting reinforcements for obtaining the synergetic effect for fast charge-transfer kinetics [16–19]. Recently, several *MXene*-supported metals were found to exhibit excellent catalytic performance for versatile reactions. For example, Li *et al.* [9] found that after the functional group of Nb<sub>2</sub>CT<sub>x</sub> (F, O, and/or OH) was removed by H<sub>2</sub> reduction at 550°C, SMSI occurred in Pt/Nb<sub>2</sub>CT<sub>x</sub> composites. Zhou *et al.* [20] synthesized a *MXene*-supported Pd catalyst and found that the activity of Pd/*MXene* toward methanol oxidation reaction was enhanced by over 60% compared with that of commercial Pd/C. They attributed the high activity to the interfacial electronic structure tuned by SMSI between Pd and *MXene*. Xu *et al.* [21] developed a *MXene* and carbon nanotube hybrid composite as supports for Pt (Pt/CNT-*MXene*). Because of the SMSI and peculiar geometry, the

\*yzx@henannu.edu.cn

†wur@uci.edu

durability of these catalysts was greatly enhanced and the mass activity toward ORR was improved 3.4 times over that of Pt/C.

Our recent work [22] reported catalytic properties of a variety of transition metals (TMs, including Ni, Pd, Pt, Cu, Ag, and Au) on V<sub>2</sub>C *MXene*. V<sub>2</sub>C was found to be an excellent support for TMs and the SMSI between them plays a crucial role in determining the morphology, stability, and activity of the catalysts. However, Ni and Cu monolayers on the support may easily be oxidized and deformed during the ORR process. Similar issues were also reported by others [23], but comprehensive studies for the stability of these TM/*MXene* structures in the reaction condition is still absent. Furthermore, the bifunctional catalytic performance toward both ORR and OER has rarely been considered to date.

In this work, focusing on the problems of high cost, low stability, and low activity, etc. of the PEMFC cathode, we systematically investigate the physical properties, stability, resistance to corrosion and bifunctional catalytic activity of Pt on different *MXenes* (Ti<sub>2</sub>C, Zr<sub>2</sub>C, Hf<sub>2</sub>C, V<sub>2</sub>C, Nb<sub>2</sub>C, Ta<sub>2</sub>C, Cr<sub>2</sub>C, Mo<sub>2</sub>C, and W<sub>2</sub>C). We address these critical issues from a physical perspective: (1) How are the geometry and electronic structure of Pt affected by the *MXene* supports? (2) What is the key factor fundamentally determining the stability of Pt/*MXene* composites? (3) Can we use a simple descriptor to screen the systems with high stability? (4) How can we achieve high ORR and OER bifunctional catalytic performances? (5) Is the proposed descriptor versatile for other TM/*MXene* composites? Answers to these questions would enrich chemical science and pave the way for the design of low-cost, stable, corrosion-resistance, and efficient bifunctional catalysts for PEMFCs and other energy applications.

## II. COMPUTATIONAL METHODS AND MODELS

### A. Computational methods

Spin-polarized density-functional-theory (DFT) calculations, with the inclusion of dispersive correction (DFTD), are conducted with the DMol<sup>3</sup> code [24]. Explicitly, the Perdew-Burke-Ernzerhof (PBE) [25] exchange-correlation functional is adopted and the Tkatchenko and Scheffler (TS) method [26] is used for the dispersion correction. The double numerical plus polarization (DNP) [27] is invoked in the atomic orbital basis set, and the DFT semicore pseudopotentials (DSPPs) [28] are adopted to represent the effect of core electrons. The convergence tolerances for geometry optimization are set as 10<sup>-5</sup>  $E_h$  for energy change, 0.002  $E_h$  /Å for the maximum force, and 0.005 Å for the maximum displacement. The conductor-like screening model (COSMO) is used to simulate a H<sub>2</sub>O solvent environment with a dielectric constant of 78.54. The threshold for self-consistent field (SCF) density convergence is set as 10<sup>-6</sup>  $E_h$ . The Monkhorst-Pack (MP)

scheme [29] is used to sample the Brillouin zone, with  $k$ -points meshes of 5 × 5 × 1 for geometry optimization and 11 × 11 × 1 for electronic structure computation. Test calculations with expanded parameters are performed to ensure the convergence of results.

The computational hydrogen electrode (CHE) model [30] is employed to calculate the Gibbs free-energy change ( $\Delta G$ ) for each elementary step of reactions. The value of  $\Delta G$  is calculated according to the following equation:

$$\Delta G = \Delta E + \Delta ZPE - T\Delta S + \Delta G_{pH} + \Delta G_U, \quad (1)$$

where  $\Delta E$  corresponds to the energy difference obtained from DFT calculations,  $\Delta ZPE$ ,  $T$ , and  $\Delta S$  are the zero-point correction, temperature (298 K), and entropy, respectively. The  $\Delta ZPE$  and  $\Delta S$  are determined by the vibrational and phonon spectra of adsorbates on substrates as presented in Tables SI and SII within the Supplemental Material [31]. The entropies of molecules in gas phase are directly taken from the National Institute for Standards and Technology (NIST) database [42].  $\Delta G_{pH}$  (=2.303 ×  $k_B T$  × pH) is the corrected free energy due to H<sup>+</sup> concentration, which is zero in the acidic media (pH=0).  $\Delta G_U$  represents the free-energy contribution due to electrode potential. To avoid the inaccuracy of DFT values [43].  $\Delta G$  of O<sub>2</sub> is determined by fitting the experimental reaction energy for O<sub>2</sub> + 2H<sub>2</sub> → 2H<sub>2</sub>O, which gives  $\Delta G$ =4.92 eV for O<sub>2</sub> at 298 K under a pressure of 0.035 bar.

The transition states and kinetic barriers for Pt migration on the overlayer and O adatom migration are simulated by complete linear synchronous transition and quadratic synchronous transit methods [44] with a rms convergence of 0.002  $E_h$ /Å.

### B. Models

To model the TM/*MXene* composites, we build a 3 × 3 M<sub>2</sub>C (M = Ti, Zr, Hf, V, Nb, Ta, Cr, Mo, and W) supercell containing 18 metal atoms and 9 carbon atoms with a vacuum of 15 Å in the  $z$  direction to avoid the interlaminar interaction. More details regarding the structure of the support are presented in the section “Details regarding the support” within the Supplemental Material [31]. Considering the symmetry of this model, three different sites on M<sub>2</sub>C are considered for the TM adatoms, i.e., fcc, hcp, and top sites, as shown in Fig. 1(a). TM atoms are added one by one and finally to a monolayer coverage on M<sub>2</sub>C, as illustrated in Figs. 1(b)–1(d). According to total energies, all TM atoms prefer the fcc sites on group 4 and 5 *MXenes* (Ti<sub>2</sub>C, V<sub>2</sub>C, Zr<sub>2</sub>C, Nb<sub>2</sub>C, Hf<sub>2</sub>C, and Ta<sub>2</sub>C) then the hcp sites on group 6 *MXenes* (Cr<sub>2</sub>C, Mo<sub>2</sub>C, and W<sub>2</sub>C).

To evaluate the impact of Pt deposition on the lattice parameters of the supports, we reoptimized the cell after Pt deposited on *MXene*, as listed in Table SIV and Fig. S1 within the Supplemental Material [31]. We find that it

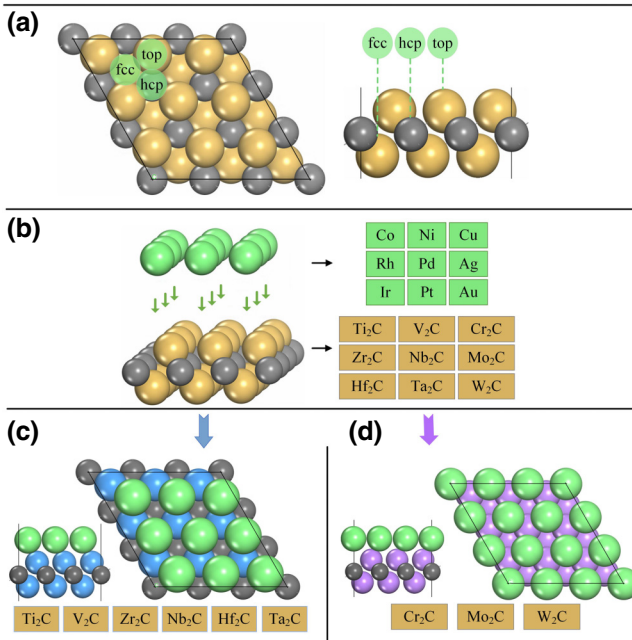


FIG. 1. (a) Top and side views of *MXene* with a general formula of  $M_2C$ . The considered sites for trapping transition metal atoms, including the fcc, hcp, and top, are filled with green. (b) The illustration of transition metals deposited on *MXenes*. (c), (d) Top and side views of the most stable  $TM_{ML}/MXenes$  composites with different configurations. The gray and yellow spheres denote the C and “M” in  $M_2C$ , respectively. The deposited transition metals are represented by green spheres. The blue spheres in (c) represent the “M” of groups 4 and 5 in  $M_2C$ , while the purple spheres in (d) stand for the “M” of group 6 in  $M_2C$ .

is negligible for the variation on the lattice parameters of  $M_2C$  before and after Pt deposition (less than 1%). Therefore, we fix the lattice parameters of the supports when TM atoms are deposited to reduce the huge calculation time consumption. More discussions on the variation of the lattice parameters are presented in the section “Details regarding the support” within the Supplemental Material [31].

### III. RESULTS AND DISCUSSION

#### A. The morphologies and electronic structures of Pt tuned by SMSI effect

Our previous studies revealed that Pt atoms can form a monolayer on  $V_2C$  [22]. To determine the morphology of Pt on other *MXenes*, we first use adhesion energy to evaluate the strength of Pt-support interaction, as follows:

$$E_{\text{adh}}(\text{Pt}) = [E(\text{Pt}_{\text{ML}}/\text{MXene}) - E(\text{MXene}) - E(\text{Pt}_{\text{ML}})]/n, \quad (2)$$

where  $E(\text{Pt}_{\text{ML}}/\text{MXene})$ ,  $E(\text{MXene})$ , and  $E(\text{Pt}_{\text{ML}})$  are the total energy of  $\text{Pt}_{\text{ML}}/\text{MXene}$ , bare *MXene*, and a

pseudomorphic freestanding Pt monolayer with the same structure as the  $\text{Pt}_{\text{ML}}$  in  $\text{Pt}_{\text{ML}}/\text{MXene}$ , respectively.  $n$  is the number of Pt atoms on *MXenes*. According to this definition, the adhesion energy of Pt on *MXene* can be used to evaluate the Pt-*MXene* bond strength not including the Pt-Pt interaction. The calculated results are listed in Table I. We find that the adhesion energies of Pt on different *MXenes* vary between  $-2.82$  and  $-4.03$  eV, suggesting strong interactions between Pt and the supports.

To evaluate the thermodynamic tendencies to mix Pt atoms and M atoms together to form intermetallic compounds, we perform the calculations of the energy difference to exchange one Pt atom in the monolayer with one M atom in  $M_2C$  just below the Pt monolayer ( $M_1\text{Pt}_{\text{ML-1}}/\text{Pt}_1\text{M}_x\text{C}_y$ ). Taking the Pt monolayer on  $V_2C$  as an example, the configurations of  $\text{Pt}_{\text{ML}}/\text{V}_2\text{C}$  and  $\text{V}_1\text{Pt}_{\text{ML-1}}/\text{Pt}_1\text{V}_x\text{C}_y$  are shown in Fig. S2 within the Supplemental Material [31] after fully geometry optimization. The total energy of  $\text{Pt}_{\text{ML}}/\text{V}_2\text{C}$  are lower than that of  $\text{V}_1\text{Pt}_{\text{ML-1}}/\text{Pt}_1\text{V}_x\text{C}_y$ , with an energy difference is  $-3.27$  eV. Besides, we calculate all the energy differences between  $\text{Pt}_{\text{ML}}/\text{M}_2\text{C}$  and  $M_1\text{Pt}_{\text{ML-1}}/\text{Pt}_1\text{M}_x\text{C}_y$ , and the values are all negative (lower than  $-1.93$  eV), as shown in Fig. S3 within the Supplemental Material [31]. The results suggest that the Pt monolayer on all the studied  $M_2\text{C}$  *MXene* are more thermodynamically stable than the structure that exchanges one Pt atom in the monolayer with one M atom in  $M_2\text{C}$ .

Next, in order to evaluate whether the Pt atoms in the monolayer tend to migrate and aggregate, we calculate the migration barrier of one Pt atom from the most stable site to the nearby metastable site, as shown in Fig. S4 and Table SV within the Supplemental Material [31]. We find that this process needs to overcome a huge energy barrier (3.44–4.12 eV) with a large endothermic energy of 2.80–3.67 eV, suggesting that the migrating of Pt atoms on the surface is both kinetically and thermodynamically unfavored. The results indicate that Pt adatoms prefer to form a monolayer rather than clusters on the *MXenes*.

To assess the dissolution and corrosion tendency of the supported layer in the electrochemical process with respect to its pure metallic phase, we calculate the dissolution energy ( $E_{\text{diss}}$ ) [45], which is defined as

$$E_{\text{diss}} = E(\text{Pt}_{\text{ML}}/\text{MXene}) - E(\text{Pt}_{\text{ML-1}}/\text{MXene}) - E(\text{Pt}), \quad (3)$$

where  $E(\text{Pt}_{\text{ML}}/\text{MXene})$ ,  $E(\text{Pt}_{\text{ML-1}}/\text{MXene})$  are the total energies of Pt/*MXene* before and after removal of one Pt atom from the Pt monolayer, respectively.  $E(\text{Pt})$  is the energy of the Pt atom in the Pt bulk. According to this definition, a negative value indicates that the Pt monolayer on *MXene* is less prone to being corroded with respect to the pure metallic phase of Pt. The calculated results are listed in Table I. We find that the dissolution energies of

TABLE I. Parameters of the Pt monolayer deposited on Ti<sub>2</sub>C, Zr<sub>2</sub>C, Hf<sub>2</sub>C, V<sub>2</sub>C, Nb<sub>2</sub>C, Ta<sub>2</sub>C, Cr<sub>2</sub>C, Mo<sub>2</sub>C, and W<sub>2</sub>C.  $\Delta q$  is the Mulliken charges per Pt atom, and a negative value suggests electron aggregation. The energy is in eV and the length is in Å.

	Ti <sub>2</sub> C	Zr <sub>2</sub> C	Hf <sub>2</sub> C	V <sub>2</sub> C	Nb <sub>2</sub> C	Ta <sub>2</sub> C	Cr <sub>2</sub> C	Mo <sub>2</sub> C	W <sub>2</sub> C
Site	fcc	fcc	fcc	fcc	fcc	fcc	hcp	hcp	hcp
$E_{\text{adh}}$	-3.80	-4.00	-4.03	-3.41	-3.91	-3.70	-2.87	-3.14	-2.82
$E_{\text{diss}}$	-2.42	-1.85	-1.94	-2.69	-2.37	-2.23	-2.77	-2.58	-2.44
$\Delta q$	-0.56	-0.51	-0.43	-0.60	-0.51	-0.37	-0.61	-0.49	-0.32

Pt on different *M*Xenes are all negative (from -2.77 to -1.85 eV), suggesting that the Pt monolayer on all the studied *M*Xenes are more corrosion resistant than Pt bulk.

From the Mulliken charges in Table I, we note that considerable electron transfer from *M*Xenes to Pt occurs, with each Pt atom obtaining 0.32 to 0.61 *e*. These electrons occupy the *d* orbitals of Pt and cause strong Coulomb attraction and hybridization between Pt and the M atoms in *M*Xenes, as also seen from the curves of partial density of states (PDOS) in Fig. S5 within the Supplemental Material [31]. This synergistic effect between Pt and *M*Xenes makes the surface rich in electrons, and is expected to improve the catalytic activity of Pt<sub>ML</sub>/*M*Xene, similar to what occurs in graphene/*M*Xene heterostructures [46], Pt/v-Ti<sub>n+1</sub>C<sub>n</sub>T<sub>2</sub> [47] and Pt/Ti<sub>3</sub>C<sub>2</sub>X<sub>2</sub> reported in experiments [48]. Besides, from Fig. S5 within the Supplemental Material [31], all the composites have good electrical conductance.

Based on the above results, we come to some conclusions: (1) The good electrical conductivity of all the composites can effectively provide electrical connection between the catalyst and the rest of the cell, which is a prerequisite for the electrode in PEMFCs and other electrochemical devices. (2) The SMSI between Pt and *M*Xene leads to the Pt atoms being highly dispersed and forming an atomically thin Pt film on *M*Xene. Compared to Pt NPs on carbon, this kind of morphology can maximize the electrocatalytic surface area and minimize the loading of Pt to reduce the cost of the materials, which is the bottleneck of PEMFCs for large-scale application. Besides, (3) the SMSI can prevent migration of Pt during long-term operations. That is, the stability and durability of the catalyst can be enhanced by SMSI, as those observed in Pt/e-TAC [6] and Pt/Nb<sub>2</sub>CT<sub>x</sub> [9]. (4) Due to significant electron transfer, the physicochemical property, especially the activity of Pt can be tuned and the *M*Xene support functions as a co-catalyst for Pt. Overall, the Pt/*M*Xene composites for the cathode in PEMFCs are expected to be able to overcome the shortcomings of the Pt/C catalyst in the above aspects.

## B. The stability of Pt<sub>ML</sub>/*M*Xene composites under reaction conditions

Now we discuss the thermal stability of the Pt monolayer *M*Xenes under reaction conditions, especially in the

presence of oxygen, which can cause severe corrosion for Pt/C (conditions with severe corrosion for Pt/C). Previous work [22,23] reported that the adsorption of O may cause severe deformation of the TM monolayer on *M*Xene and destabilize the composites. Here, we explore the effect of O adsorption on Pt<sub>ML</sub>/*M*Xene. After considering all possible adsorption sites, the most stable configurations of oxygen on different Pt<sub>ML</sub>/*M*Xenes are shown in Fig. 2. We find that the Pt monolayers on Ti<sub>2</sub>C, Zr<sub>2</sub>C, Hf<sub>2</sub>C, Nb<sub>2</sub>C, and Ta<sub>2</sub>C are deformed because of O adsorption. The O atom sinks into the monolayer and directly binds to the M atom in *M*Xene, causing damage to the Pt monolayer. In contrast, the structures of Pt monolayers on V<sub>2</sub>C, Cr<sub>2</sub>C, Mo<sub>2</sub>C, and W<sub>2</sub>C are well maintained after the adsorption of O atoms. The O atoms are adsorbed above the Pt monolayer and form O-Pt triple coordinates. These results indicate that the stability of the Pt monolayer depends on the *M*Xene substrates.

It is crucial to know the influence of additional O atoms on the stability and activity of the Pt monolayer. Taking Pt<sub>ML</sub>/Nb<sub>2</sub>C as an example, the O atom spontaneously sinks under the Pt monolayer and directly binds to Nb after the structural optimization procedure as shown in Fig. 2(e), even we initially place it above the Pt monolayer. More O atoms also sink, as shown in Fig. S6 within the Supplemental Material [31]. To evaluate the impact of sinking O atoms on the binding strength of Pt, the binding energy of Pt atom in the Pt monolayer with *n* O atom(s) sink in (Pt<sub>ML</sub>O<sub>*n*</sub>/*M*Xene) is calculated as follows:

$$E_{\text{b-O}}(\text{Pt}) = E(\text{Pt}_\text{ML} \text{O}_n / \text{MXene}) - E(\text{Pt}_\text{ML-1} \text{O}_n / \text{MXene}) - E(\text{Pt}), \quad (4)$$

where  $E(\text{Pt}_\text{ML} \text{O}_n / \text{MXene})$  and  $E(\text{Pt}_\text{ML-1} \text{O}_n / \text{MXene})$  are the total energies of systems with a complete Pt monolayer and a defective Pt monolayer with one Pt atom missing, respectively.  $E(\text{Pt})$  is the total energy of one isolated Pt atom. From Fig. 3(a), we find that the binding energy of Pt decreases with the number of O atoms under Pt increases. Obviously, the cumulation of O atoms under the Pt monolayer should be prevented, even their harm on the stability is still manageable (with a binding energy larger than 6 eV per Pt atom). With the presence of O atoms, the Pt-Nb bond is weakened and the coordination of Pt is changed after O

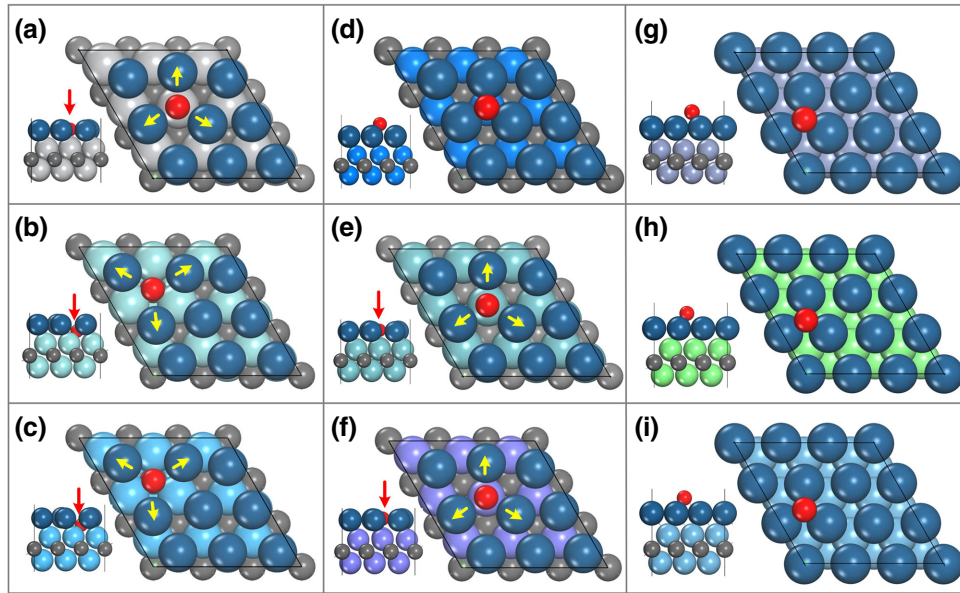


FIG. 2. Top and side views of O atom adsorbed on (a)  $\text{Pt}_{\text{ML}}/\text{Ti}_2\text{C}$ , (b)  $\text{Pt}_{\text{ML}}/\text{Zr}_2\text{C}$ , (c)  $\text{Pt}_{\text{ML}}/\text{Hf}_2\text{C}$ , (d)  $\text{Pt}_{\text{ML}}/\text{V}_2\text{C}$ , (e)  $\text{Pt}_{\text{ML}}/\text{Nb}_2\text{C}$ , (f)  $\text{Pt}_{\text{ML}}/\text{Ta}_2\text{C}$ , (g)  $\text{Pt}_{\text{ML}}/\text{Cr}_2\text{C}$ , (h)  $\text{Pt}_{\text{ML}}/\text{Mo}_2\text{C}$ , and (i)  $\text{Pt}_{\text{ML}}/\text{W}_2\text{C}$ . The gray, blue, and red spheres stand for C, Pt, and O atoms, respectively. Spheres in other colors signify different transition metals in MXenes. The red arrows indicate that the O atom has sunk into the Pt monolayer and the yellow arrows suggest the deformation of the Pt monolayer after the adsorption of O atoms.

occupies the top side of Nb. This is also evidenced by electron transfer, as shown in Fig. S7 within the Supplemental Material [31]. The competition between O and Pt leads to the result that the closer the Pt atom is to the O atom, the fewer electrons on them. From Fig. 3(b), we find that the 5d states of Pt are lower than that of Pt in pristine  $\text{Pt}_{\text{ML}}/\text{Nb}_2\text{C}$ , indicating that the activity of Pt around O also decreases.

The availability of mobile O atoms on the catalyst surface is crucial for ORR and OER. We calculate the adsorption energies of O atoms on  $\text{Pt}_{\text{ML}}/\text{MXene}$  by

$$E_{\text{ads}}(\text{O}) = E(\text{O}/\text{substrates}) - E(\text{substrates}) - E(\text{O}), \quad (5)$$

where  $E(\text{O}/\text{substrates})$  and  $E(\text{substrates})$  are the total energies of  $\text{Pt}_{\text{ML}}/\text{MXene}$  with and without O atom;  $E(\text{O})$  represents the total energy of a free O atom. The calculated results are shown in Fig. S8 within the Supplemental Material [31]. The adsorption energies of O atoms on the deformed Pt monolayer ( $-5.41$  to  $-4.34$  eV) are much lower than those on the undeformed Pt ( $-4.21$  to  $-3.76$  eV) and on Pt(111) ( $-4.13$  eV [22],  $-3.96$  eV [49]). According to the Sabatier principle [50], the catalytic activity is related to the binding strength of key reaction intermediates, and a moderate binding strength can lead to high activity. On the benchmark Pt(111), the rate-determining step of ORR is O hydrogenation because of the strong adsorption of the O atom [30]. The results indicate that the deformation of the Pt monolayer has a great influence on the adsorption strength of O, and may ultimately hinder the ORR-OER processes. On the other hand, the adsorption energies of O atoms on  $\text{Pt}_{\text{ML}}/\text{V}_2\text{C}$ ,  $\text{Pt}_{\text{ML}}/\text{Cr}_2\text{C}$ ,  $\text{Pt}_{\text{ML}}/\text{Mo}_2\text{C}$ , and  $\text{Pt}_{\text{ML}}/\text{W}_2\text{C}$  are comparable

to that on Pt(111), indicating that they are suitable for ORR-OER catalysis.

### 1. Reasons for the difference in deformation

Taking  $\text{V}_2\text{C}$  as an example, we calculate the O atom adsorbed on  $\text{V}_2\text{C}$  with and without the Pt monolayer, as shown in Figs. 4(a) and 4(b), respectively. Similar to the O-Pt three-coordinate structure of O on Pt monolayer, the O atom directly bonds to three V atoms on bare  $\text{V}_2\text{C}$ . However, the adsorption strength of O on bare  $\text{V}_2\text{C}$  is much stronger than that on the Pt monolayer ( $-8.31$  vs  $-3.76$  eV), with more electrons transfer to the adsorbed O atom ( $-0.72$  vs  $-0.64$ ). The results indicate that the chemical activity of the  $\text{V}_2\text{C}$  surface is excessively high, which can be alleviated by covering a Pt monolayer to decrease the activity and block O atom directly bonding to V atoms. Although O can be detained in the Pt monolayer in the case where it is initially placed on V below Pt, as shown in Fig. 4(c), it will go above the Pt monolayer after overcoming a negligible energy barrier ( $0.004$  eV) with an exothermic energy of  $0.53$  eV. If we further apply in-plane tensile strain on  $\text{Pt}_{\text{ML}}/\text{V}_2\text{C}$  to increase the lattice parameters ( $a$ ) from  $2.86$  to  $3.01$  Å, as shown in Fig. 4(c), the O atom will spontaneously sink into the Pt monolayer, similar to the configurations of O on  $\text{Pt}_{\text{ML}}/\text{Nb}_2\text{C}$  ( $a = 3.09$  Å). For more  $\text{Pt}_{\text{ML}}/\text{MXene}$  composites in Fig. 2, we note that the lattice parameters of MXenes ( $3.01$ – $3.12$  Å) on which the Pt monolayer is deformed are obviously larger than those of other MXenes ( $2.72$ – $2.87$  Å) on which the Pt monolayer is not deformed. The above results suggest that the lattice parameters of MXenes play a crucial role in the thermal stability of  $\text{Pt}_{\text{ML}}/\text{MXene}$  composites, and only if the surface of MXene is covered with Pt atoms tightly

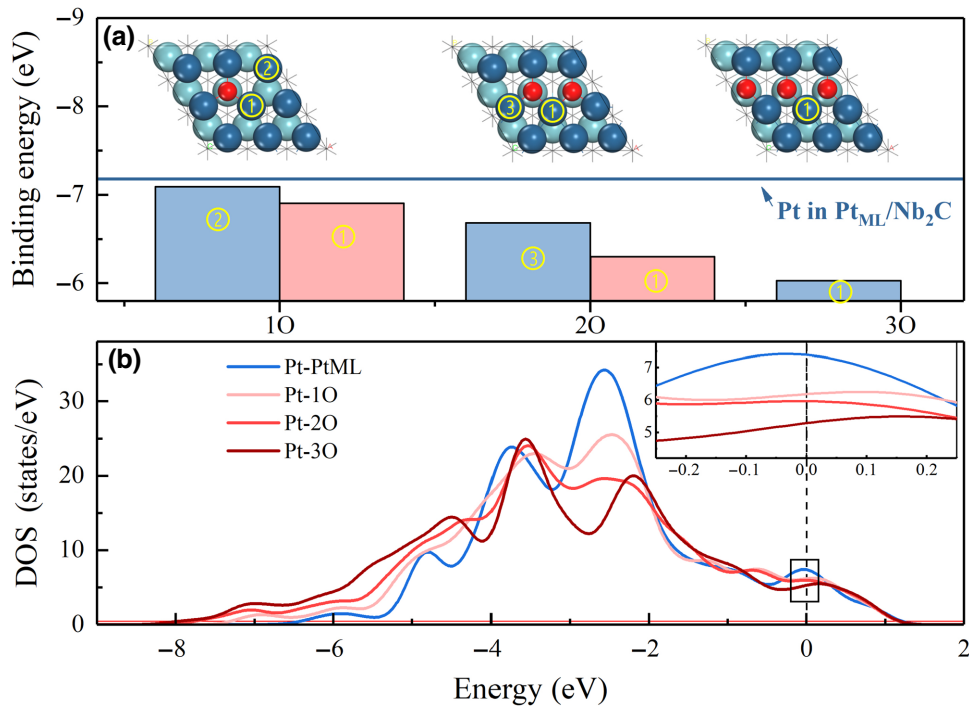


FIG. 3. (a) The binding energies of the labeled Pt atom(s). The blue line indicates the binding energy of Pt in  $\text{Pt}_{\text{ML}}/\text{Nb}_2\text{C}$  without O adsorption. (b) The DOS of 5d state of Pt in the systems of  $\text{Pt}_{\text{ML}}/\text{Nb}_2\text{C}$  with 1, 2, and 3 O atom(s).

enough will it block O sinking and maintain the stability of the Pt monolayer.

## 2. The descriptor to identify the stability

To examine the relationship between the lattice parameter and the stability, we analyze the geometry of

$\text{O-Pt}_{\text{ML}}/\text{MXene}$  as marked with the red triangle in Figs. 5(a) and 5(b). The distance between two adjacent Pt atoms equals the lattice parameter of the unit cell of MXene,  $a$ . Accordingly, the shortest distance between the O atom and its neighboring Pt atom is  $a/\sqrt{3}$  in the XY plane.

If the sum of the radii of O and Pt atoms is greater

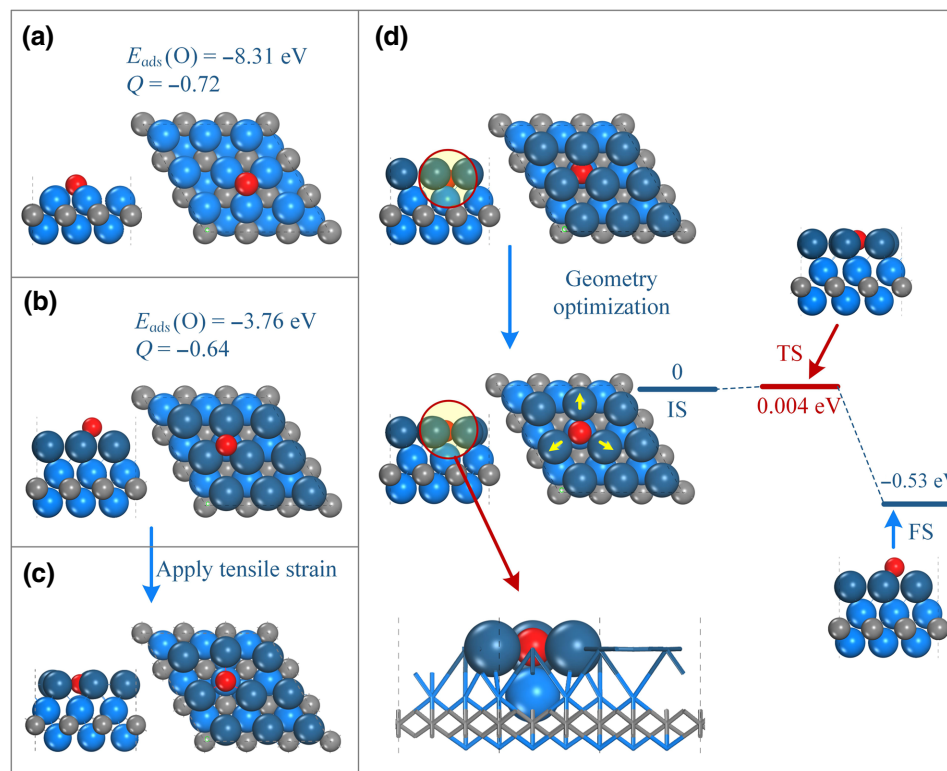


FIG. 4. The adsorption of O on bare  $\text{V}_2\text{C}$  (a) as well as  $\text{Pt}_{\text{ML}}/\text{V}_2\text{C}$  with (b) and without (c) tensile strain. (d) The configurations of  $\text{O-Pt}_{\text{ML}}/\text{V}_2\text{C}$  before and after geometry optimization in the case that an O atom is initially placed on M below Pt.

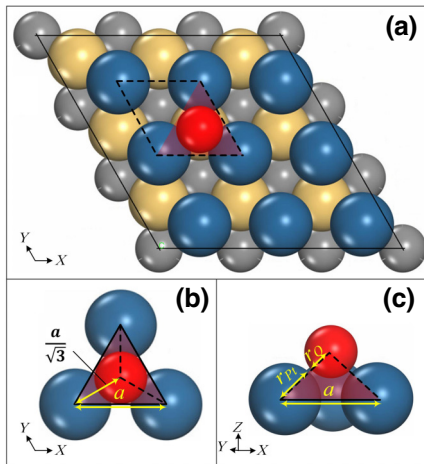


FIG. 5. (a) Top view of configuration of O adsorbed on  $\text{Pt}_{\text{ML}}/\text{MXene}$ . The area enclosed by dashed lines denotes a unit cell of  $\text{Pt}_{\text{ML}}/\text{MXene}$ . (b) Top and (c) side views of the red area. The  $a$ ,  $r_{\text{Pt}}$ , and  $r_{\text{O}}$  in the figure symbolize the lattice parameter of  $\text{MXene}$ , the radii of Pt and O atoms, respectively. The yellow sphere signifies the transition metals in  $\text{MXene}$ .

than  $a/\sqrt{3}$ , i.e.,  $\beta = r_{\text{Pt}} + r_{\text{O}} - a/\sqrt{3} > 0$ , the O atoms are likely blocked. By calculated the values of  $\beta$  for  $\text{Pt}_{\text{ML}}/\text{V}_2\text{C}$  composites, as shown in Fig. S9 and Table SVI [31] within the Supplemental Material, we find that the actual condition is  $\beta > 0.4$  for stable  $\text{Pt}_{\text{ML}}/\text{V}_2\text{C}$  composites. If  $\beta < 0.4$  (0.33–0.39), i.e., Pt monolayers on

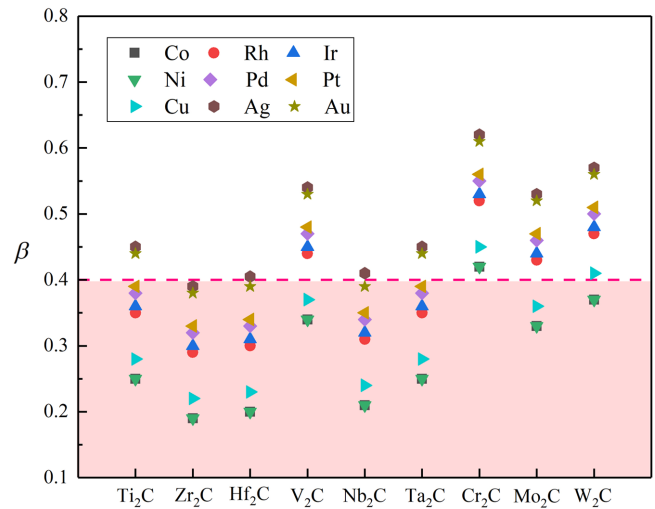


FIG. 6. Plot of  $\beta$  for various  $\text{TM}_{\text{ML}}/\text{MXene}$  composites. The symbols fall in the light red area below the dashed line at  $\beta = 0.40$  represent the predicted unstable composites.

$\text{Ti}_2\text{C}$ ,  $\text{Zr}_2\text{C}$ ,  $\text{Hf}_2\text{C}$ ,  $\text{Nb}_2\text{C}$ , and  $\text{Ta}_2\text{C}$ , the Pt monolayers are deformed by oxygen; whereas they are stable when  $\beta > 0.4$  (0.47–0.56), i.e., Pt monolayers on  $\text{V}_2\text{C}$ ,  $\text{Cr}_2\text{C}$ ,  $\text{Mo}_2\text{C}$ , and  $\text{W}_2\text{C}$ . Accordingly, we set a descriptor for the stability of  $\text{Pt}_{\text{ML}}/\text{MXene}$  composites under reaction conditions as

$$r_{\text{Pt}} + r_{\text{O}} - a/\sqrt{3} > 0.40. \quad (6)$$

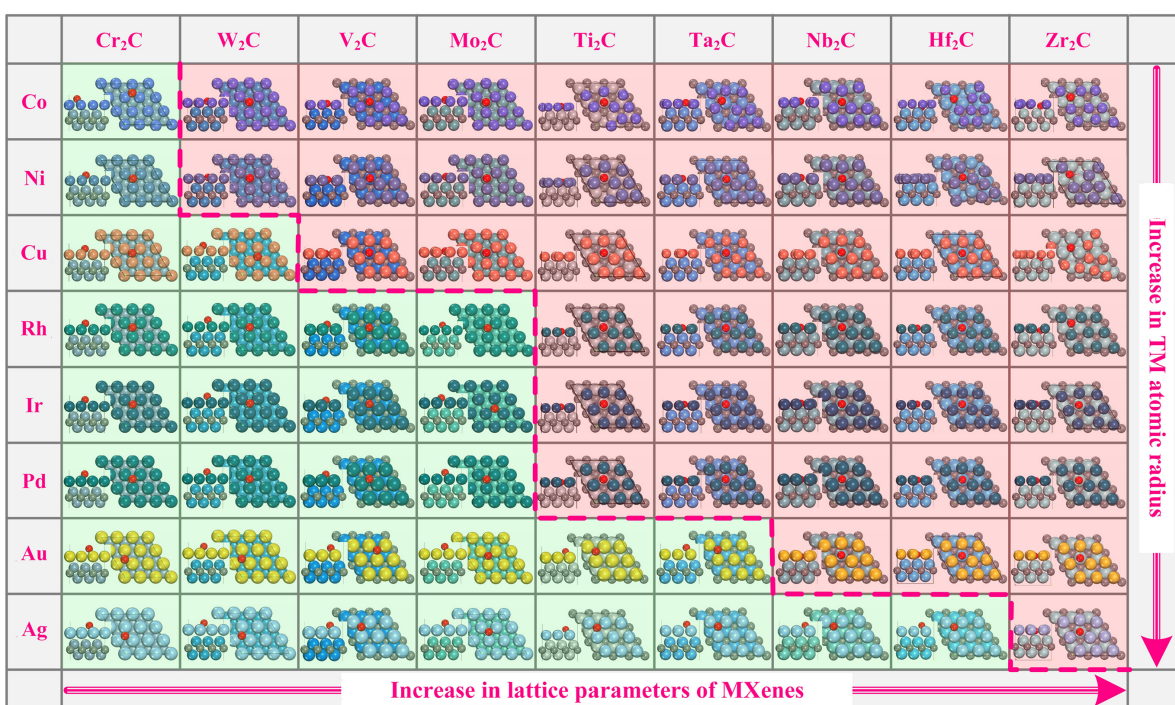


FIG. 7. Side and top views of the configuration of O adsorbed on  $\text{TM}_{\text{ML}}/\text{MXenes}$ . The composites in the light red area are deformed due to oxygen adsorption, whereas the composites in the light blue area are maintained stable.

### 3. Universality of the descriptor

To further verify the universality of the proposed descriptor, we systematically explore the stability of 81 different  $\text{TM}_{\text{ML}}/\text{MXene}$  composites ( $\text{TM} = \text{Co}, \text{Rh}, \text{Ir}, \text{Ni}, \text{Pd}, \text{Pt}, \text{Cu}, \text{Ag}, \text{and Au}; \text{MXenes} = \text{Ti}_2\text{C}, \text{Zr}_2\text{C}, \text{Hf}_2\text{C}, \text{V}_2\text{C}, \text{Nb}_2\text{C}, \text{Ta}_2\text{C}, \text{Cr}_2\text{C}, \text{Mo}_2\text{C}, \text{and W}_2\text{C}$ ). For different TM atoms, Eq. (4) can be rewritten as

$$r_{\text{TM}} + r_O - a/\sqrt{3} > 0.40.$$

Based on the descriptor, the values of  $\beta$  for the composites we study are calculated and shown in Table S VI within the Supplemental Material [31]. As discussed above, the composites are predicted to be poisoned by oxygen in the case of  $\beta < 0.4$  and shown in red in Fig. 6. For  $\text{Ti}_2\text{C}$  and  $\text{Ta}_2\text{C}$ , only Au and Ag deposited MXenes have high chemical stability because of the relatively large radii among the selected TM atoms. For  $\text{Hf}_2\text{C}$  and  $\text{Nb}_2\text{C}$ , only Ag deposited is expected to remain stable in an oxygen environment. Particularly, no  $\text{TM}_{\text{ML}}/\text{Zr}_2\text{C}$  composites are predicted to be stable because of the largest lattice parameter of  $\text{Zr}_2\text{C}$  among the studied MXenes. In contrast, most TM supported on  $\text{V}_2\text{C}, \text{Cr}_2\text{C}, \text{Mo}_2\text{C}$ , and  $\text{W}_2\text{C}$  are predicted to remain stable attributed to the relatively small lattice parameters of  $\text{V}_2\text{C}, \text{Cr}_2\text{C}, \text{Mo}_2\text{C}$ , and  $\text{W}_2\text{C}$  (2.72–2.87 Å).

To confirm the above predictions, we calculate the geometry configurations of oxygen atom adsorbed on all composites we study, as shown in Fig. 7 and Figs. S10–S18 within the Supplemental Material [31]. The TM-monolayer deformations with oxygen atoms sunk in can be obviously observed from the configurations. By comparison of Figs. 6 and 7, we find that the calculated results are consistent with the results predicted by the descriptor, and thus confirm the reliability and universality of the descriptor.

Besides, taking  $\text{TM}_{\text{ML}}/\text{V}_2\text{C}$  as a representation, we calculate the thermodynamics and kinetics of the O adatom diffusion to the subsurface in cases where  $\beta > 0.4$ . From Figs. 6 and 7, Rh, Ir, Pd, Pt, Ag, and Au TM monolayers on  $\text{V}_2\text{C}$  are supposed to be stable, i.e.,  $\beta > 0.4$ ; while the Co, Ni, and Cu monolayer on  $\text{V}_2\text{C}$  are unstable, i.e.,  $\beta < 0.4$ . For the Rh, Ir, Pd, Pt, Ag, and Au monolayer on  $\text{V}_2\text{C}$ , the thermodynamics and kinetics of the O adatom diffusion to the subsurface are shown in Fig. S19 within the Supplemental Material [31]. We find that this process needs to overcome an energy barrier by 0.54–1.40 eV with an endothermic energy of 0.22–0.91 eV, suggesting that this process is both kinetically and thermodynamically unfavored. Contrastingly, For the Co, Ni, and Cu monolayer on  $\text{V}_2\text{C}$  ( $\beta < 0.4$ ), the O atom will spontaneously sink into the TM monolayer even if we initially place it above the monolayer, as shown in Fig. S20 within the Supplemental Material [31]. In other words, there are no stable configurations of O adsorbed above Co, Ni, and Cu monolayer on  $\text{V}_2\text{C}$ . From what we discuss above, we can rationally conclude that, in view of thermodynamics and kinetics, the  $\text{TM}_{\text{ML}}/\text{MXene}$  with  $\beta > 0.4$  are more stable than those with  $\beta < 0.4$  in the case of O adsorbed on the TM monolayer.

It should be noted that the above predictions and verifications are based on the premise that TM deposition has little effect on the lattice parameters of MXene. Considering the huge computational cost, we verify only that Pt deposition has little effect on the lattice constants of MXene, the impact of other TM atoms' deposition on the lattice parameters still needs to be carefully checked.

The predicted composites with high stability may have diverse potential catalysis applications and some of which have been demonstrated to possess high stability and catalytic activity in our previous works. For example, Cheng

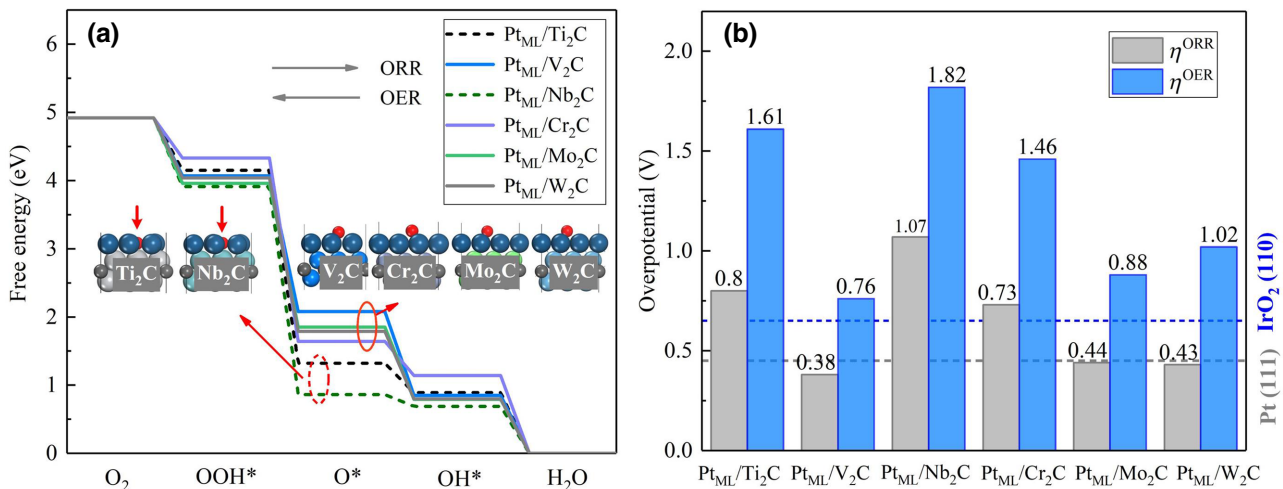


FIG. 8. Free-energy diagrams at zero electrode potential (a) and the overpotentials (b) of ORR and OER on different  $\text{Pt}_{\text{ML}}/\text{MXenes}$  composites. The blue and black dotted lines in (b) represent the overpotentials of ORR on Pt (111) and OER on  $\text{IrO}_2$ (110), respectively.

TABLE II. The adsorption free energy ( $\Delta G$ ) of OOH\*, OH\*, and O\* (in eV) on the Pt<sub>ML</sub>/MXene surface.

Species	Pt <sub>ML</sub> /Ti <sub>2</sub> C	Pt <sub>ML</sub> /V <sub>2</sub> C	Pt <sub>ML</sub> /Nb <sub>2</sub> C	Pt <sub>ML</sub> /Cr <sub>2</sub> C	Pt <sub>ML</sub> /Mo <sub>2</sub> C	Pt <sub>ML</sub> /W <sub>2</sub> C
$\Delta G_{\text{OOH}^*}$	4.15	4.07	3.91	4.33	3.96	4.04
$\Delta G_{\text{O}^*}$	1.32	2.08	0.86	1.64	1.85	1.79
$\Delta G_{\text{OH}^*}$	0.89	0.85	0.69	1.14	0.79	0.80

*et al.* [23] speculated that Au<sub>ML</sub>/Mo<sub>2</sub>C has enhanced durability and remarkable activity toward ORR compared with Pt/C catalysts. In another work [51], the authors found that Ag<sub>ML</sub>/Mo<sub>2</sub>C is an efficient catalyst for preferential oxidation of CO with low cost, high activity, selectivity and stability, which can be served as a promising hydrogen purifying pretreater connected to the anode of PEMFCs. Xu *et al.* [52] explored a series of transition metals deposited on niobium carbide MXene and screened out Ag<sub>ML</sub>/Nb<sub>2</sub>C as an excellent catalyst for CO oxidation with an energy barrier of 0.35 eV for rate-determining steps (RDS). Besides, the properties and applications of more TM<sub>ML</sub>/MXenes composites required in-depth investigations by experimental and theoretical approaches.

### C. The ORR-OER bifunctional catalytic activity of Pt<sub>ML</sub>/MXene

Catalysts for ORR and OER are the essential components of renewable energy devices, including fuel cells and water splitting [53]. Currently, noble metal-based materials are used as catalysts in practical applications, with Pt for ORR and RuO<sub>2</sub> and IrO<sub>2</sub> for OER [41,54,55]. However, sluggish ORR kinetics demands a large amount of noble metal loading, leading to an increase in the overall cost of these renewable energy devices. Moreover, they are incapable of simultaneously catalyzing ORR and OER [56,57]. Here, we discuss the ORR-OER bifunctional catalytic activity of Pt<sub>ML</sub>/MXene.

According to the theory proposed by Nørskov *et al.* [30], the four-electron electrochemical reaction processes of ORR and OER were simulated in an acidic environment with zero electrode potential, as shown in Fig. 8. The calculated adsorption free energies of key intermediates involved in ORR and OER are listed in Table II. More computational details are presented within the Supplemental Material [31]. We find that the adsorption free energies of O on Pt<sub>ML</sub>/Ti<sub>2</sub>C (1.32 eV) and Pt<sub>ML</sub>/Nb<sub>2</sub>C (0.86 eV) are obviously lower than those on the other substrates (1.64–2.08 eV). As discussed above, the strong binding of O prevents the subsequent reaction processes. This point can be elucidated from energy diagrams in Fig. 8(a) and Table SVII within the Supplemental Material [31], where the RDS of ORR and OER on Pt<sub>ML</sub>/Ti<sub>2</sub>C and Pt<sub>ML</sub>/Nb<sub>2</sub>C are the formation of OH\* and OOH\* from O\*, respectively.

Figure 8(b) presents the overpotentials of ORR and OER on different Pt<sub>ML</sub>/MXene composites. As the benchmark

systems, the overpotential of ORR on Pt (111) and overpotential of OER on IrO<sub>2</sub>(110) are also given in Fig. 8(b), which are generally considered as the reference electrocatalysts in experiments. The systems that are stable during the reaction, i.e., Pt<sub>ML</sub>/V<sub>2</sub>C, Pt<sub>ML</sub>/Cr<sub>2</sub>C, Pt<sub>ML</sub>/Mo<sub>2</sub>C, and Pt<sub>ML</sub>/W<sub>2</sub>C, exhibit relatively superior catalytic activity toward ORR and OER and many of them might be potential ORR-OER bifunctional catalysts. The best case is Pt<sub>ML</sub>/V<sub>2</sub>C, which not only exhibits a lower ORR overpotential than that of Pt (111) (0.38 vs 0.45 V [30]), but also has a comparable OER overpotential to that of IrO<sub>2</sub> (0.76 vs 0.65 V [58]). In contrast, the unstable systems such as Pt<sub>ML</sub>/Ti<sub>2</sub>C and Pt<sub>ML</sub>/Nb<sub>2</sub>C have poor activity for both ORR (0.8–1.07 eV) and OER (1.61–1.82 eV), due to the overbinding of O. These results demonstrate that the deformation of the Pt monolayer during the reaction process can significantly deteriorate the catalytic activity.

### IV. CONCLUSIONS

In short, starting from the problems existing in the cathode catalysts of PEMFCs, we extensively explore the physical properties, stability, and ORR-OER bifunctional catalytic activity of Pt supported on MXene using theoretical approach. The SMSI between Pt and MXenes stabilizes the monolayer adsorption geometry and alters the electronic structure of Pt. This increases the utilization of noble metals and allows tuning the catalytic activity of these heterostructures in a wide range. By analyzing the chemical stability of Pt monolayers on different MXenes, we find that the lattice parameter of MXenes plays a crucial role in governing the stability of the composites and a descriptor is proposed accordingly. By examining nine TMs supported on nine MXenes (81 composites in total), we find that the simple descriptor we propose is effective and universal to screen the stable TM/MXene composites. The undeformed Pt/MXene combinations have a good potential for ORR-OER applications. Particularly, Pt/V<sub>2</sub>C exhibits the best bifunctional catalytic activity, with the overpotentials of 0.38 (ORR) and 0.76 V (OER), respectively. From a fresh physics view, this study provides useful guidance for the design of low-cost, highly stable, and active catalysts in the cathode of PEMFCs based on MXene and suggests several promising metal-MXene catalysts for experimental verification. We hope this study will have a far-reaching effect on the development of fuel cells.

## ACKNOWLEDGMENTS

This work is supported by the National Natural Science Foundation of China (Grants No. U1804130, No. 11874141, No. 11904084, and No. U2004212), Henan Overseas Expertise Introduction Center for Discipline Innovation (Grant No. CXJD2019005). The simulations are performed on resources provided by the High Performance Computing Center of Henan Normal University.

- 
- [1] M. Armand and J. M. Tarascon, Building better batteries, *Nature* **451**, 652 (2008).
  - [2] Y. Shao-Horn, W. C. Sheng, S. Chen, P. J. Ferreira, E. F. Holby, and D. Morgan, Instability of supported platinum nanoparticles in Low-temperature fuel cells, *Top. Catal.* **46**, 285 (2007).
  - [3] K. Sasaki, N. Marinkovic, H. S. Isaacs, and R. R. Adzic, Synchrotron-Based In situ characterization of carbon-supported platinum and platinum monolayer electrocatalysts, *ACS Catal.* **6**, 69 (2016).
  - [4] S. Sui, X. Wang, X. Zhou, Y. Su, S. Riffat, and C.-j. Liu, A comprehensive review of Pt electrocatalysts for the oxygen reduction reaction: Nanostructure, activity, mechanism and carbon support in PEM fuel cells, *J. Mater. Chem. A* **5**, 1808 (2017).
  - [5] L. Li, L. Hu, J. Li, and Z. Wei, Enhanced stability of Pt nanoparticle electrocatalysts for fuel cells, *Nano Res.* **8**, 418 (2015).
  - [6] X. Xie, Y. Xue, L. Li, S. Chen, Y. Nie, W. Ding, and Z. Wei, Surface Al leached Ti<sub>3</sub>AlC<sub>2</sub> as a substitute for carbon for use as a catalyst support in a harsh corrosive electrochemical system, *Nanoscale* **6**, 11035 (2014).
  - [7] N. Cheng, M. Norouzi Banis, J. Liu, A. Riese, S. Mu, R. Li, T.-K. Sham, and X. Sun, Atomic scale enhancement of metal–support interactions between Pt and ZrC for highly stable electrocatalysts, *Energy Environ. Sci.* **8**, 1450 (2015).
  - [8] S.-A. Park, D.-S. Kim, T.-J. Kim, and Y.-T. Kim, Strong interaction between Pt and thiolated carbon for electrocatalytic durability enhancement, *ACS Catal.* **3**, 3067 (2013).
  - [9] Z. Li, Y. Cui, Z. Wu, C. Milligan, L. Zhou, G. Mitchell, B. Xu, E. Shi, J. T. Miller, F. H. Ribeiro, et al., Reactive metal–support interactions at moderate temperature in two-dimensional niobium-carbide-supported platinum catalysts, *Nat. Catal.* **1**, 349 (2018).
  - [10] Z. Li, L. Yu, C. Milligan, T. Ma, L. Zhou, Y. Cui, Z. Qi, N. Libretto, B. Xu, J. Luo, et al., Two-dimensional transition metal carbides as supports for tuning the chemistry of catalytic nanoparticles, *Nat. Commun.* **9**, 5258 (2018).
  - [11] B. Anasori, M. R. Lukatskaya, and Y. Gogotsi, 2D metal carbides and nitrides (MXenes) for energy storage, *Nat. Rev. Mater.* **2**, 16098 (2017).
  - [12] M. Naguib, O. Mashtalir, J. Carle, V. Presser, J. Lu, L. Hultman, Y. Gogotsi, and M. W. Barsoum, Two-Dimensional transition metal carbides, *ACS Nano* **6**, 1322 (2012).
  - [13] X. Liang, A. Garsuch, and L. F. Nazar, Sulfur cathodes based on conductive MXene nanosheets for high-performance lithium–sulfur batteries, *Angew. Chem., Int. Ed.* **54**, 3907 (2015).
  - [14] X. Wang, S. Kajiyama, H. Iinuma, E. Hosono, S. Oro, I. Moriguchi, M. Okubo, and A. Yamada, Pseudocapacitance of MXene nanosheets for high-power sodium-ion hybrid capacitors, *Nat. Commun.* **6**, 6544 (2015).
  - [15] A. Champagne, L. Shi, T. Ouisse, B. Hackens, and J.-C. Charlier, Electronic and vibrational properties of V<sub>2</sub>C-based MXenes: From experiments to first-principles modeling, *Phys. Rev. B* **97**, 115439 (2018).
  - [16] X. Wu, Z. Wang, M. Yu, L. Xiu, and J. Qiu, Stabilizing the MXenes by carbon nanoploting for developing hierarchical nanohybrids with efficient lithium storage and hydrogen evolution capability, *Adv. Mater.* **29**, 1607017 (2017).
  - [17] Z. Zhang, H. Li, G. Zou, C. Fernandez, B. Liu, Q. Zhang, J. Hu, and Q. Peng, Self-Reduction synthesis of New MXene/Ag composites with unexpected electrocatalytic activity, *ACS Sustainable Chem. Eng.* **4**, 6763 (2016).
  - [18] X. Yu, W. Yin, T. Wang, and Y. Zhang, Decorating g-C<sub>3</sub>N<sub>4</sub> nanosheets with Ti<sub>3</sub>C<sub>2</sub> MXene nanoparticles for efficient oxygen reduction reaction, *Langmuir* **35**, 2909 (2019).
  - [19] Z. Li, Z. Zhuang, F. Lv, H. Zhu, L. Zhou, M. Luo, J. Zhu, Z. Lang, S. Feng, W. Chen, et al., The marriage of the FeN<sub>4</sub> moiety and MXene boosts oxygen reduction catalysis: Fe 3d electron delocalization matters, *Adv. Mater.* **30**, 1803220 (2018).
  - [20] Z. Lang, Z. Zhuang, S. Li, L. Xia, Y. Zhao, Y. Zhao, C. Han, and L. Zhou, MXene surface terminations enable strong metal–support interactions for efficient methanol oxidation on palladium, *ACS Appl. Mater. Interfaces* **12**, 2400 (2020).
  - [21] C. Xu, C. Fan, X. Zhang, H. Chen, X. Liu, Z. Fu, R. Wang, T. Hong, and J. Cheng, MXene (Ti<sub>3</sub>C<sub>2</sub>T<sub>x</sub>) and carbon nanotube hybrid-supported platinum catalysts for the high-performance oxygen reduction reaction in PEMFC, *ACS Appl. Mater. Interfaces* **12**, 19539 (2020).
  - [22] X. Yang, Y. Zhang, Z. Fu, Z. Lu, X. Zhang, Y. Wang, Z. Yang, and R. Wu, Tailoring the electronic structure of transition metals by the V<sub>2</sub>C MXene support: Excellent oxygen reduction performance triggered by metal–support interactions, *ACS Appl. Mater. Interfaces* **12**, 28206 (2020).
  - [23] C. Cheng, X. Zhang, Z. Fu, and Z. Yang, Strong metal–support interactions impart activity in the oxygen reduction reaction: Au monolayer on Mo<sub>2</sub>C (MXene), *J. Phys.: Condens. Matter* **30**, 475201 (2018).
  - [24] B. Delley, D. E. Ellis, A. J. Freeman, E. J. Baerends, and D. Post, Binding energy and electronic structure of small copper particles, *Phys. Rev. B* **27**, 2132 (1983).
  - [25] J. P. Perdew, K. Burke, and M. Ernzerhof, Generalized gradient approximation made simple, *Phys. Rev. Lett.* **77**, 3865 (1996).
  - [26] A. Tkatchenko and M. Scheffler, Accurate molecular Van Der Waals interactions from ground-state electron density and free-atom reference data, *Phys. Rev. Lett.* **102**, 073005 (2009).
  - [27] B. Delley, Ground-State enthalpies: evaluation of electronic structure approaches with emphasis on the density functional method, *J. Phys. Chem. A* **110**, 13632 (2006).
  - [28] B. Delley, Hardness conserving semilocal pseudopotentials, *Phys. Rev. B* **66**, 155125 (2002).
  - [29] H. J. Monkhorst and J. D. Pack, Special points for brillouin-zone integrations, *Phys. Rev. B* **13**, 5188 (1976).

- [30] J. K. Nørskov, J. Rossmeisl, A. Logadottir, L. Lindqvist, J. R. Kitchin, T. Bligaard, and H. Jónsson, Origin of the overpotential for oxygen reduction at a fuel-cell cathode, *J. Phys. Chem. B* **108**, 17886 (2004).
- [31] See Supplemental Material, which includes Refs. [11, 22,30,32–41], at <http://link.aps.org/supplemental/10.1103/PhysRevApplied.15.044053> for details regarding the support; Pt migration on Pt/MXene; the calculated values of  $b$  for TM<sub>ML</sub>/MXenes; the energy difference between Pt<sub>ML</sub>/V<sub>2</sub>C and V<sub>1</sub>Pt<sub>ML-1</sub>/Pt<sub>1</sub>V<sub>x</sub>C<sub>y</sub> as well as Pt<sub>ML</sub>/M<sub>2</sub>C and M<sub>1</sub>Pt<sub>ML-1</sub>/Pt<sub>1</sub>M<sub>x</sub>C<sub>y</sub>; the configurations of 1–3 O atoms on Pt<sub>ML</sub>/Nb<sub>2</sub>C and the DOS of 5d state of Pt atoms closest to O atoms; the adsorption energy of O on Pt<sub>ML</sub>/MXenes; the configurations of O atom on Co, Ni, Cu, Rh, Pd, Ag, Ir, and Au monolayer deposited on MXenes; the diffusion pathway of the O adatom from above to below the TM monolayer on V<sub>2</sub>C; the configurations of O on Co<sub>ML</sub>/V<sub>2</sub>C, Ni<sub>ML</sub>/V<sub>2</sub>C, and Cu<sub>ML</sub>/V<sub>2</sub>C, and more computational details related to ORR and OER.
- [32] V. Kamysbayev, A. S. Filatov, H. Hu, X. Rui, F. Lagunas, D. Wang, R. F. Klie, and D. V. Talapin, Covalent surface modifications and superconductivity of two-dimensional metal carbide MXenes, *Science* **369**, 979 (2020).
- [33] M. Kurtoglu, M. Naguib, Y. Gogotsi, and M. W. Barsoum, First principles study of two-dimensional early transition metal carbides, *MRS Commun.* **2**, 133 (2012).
- [34] C. Chen, X. Ji, K. Xu, B. Zhang, L. Miao, and J. Jiang, Prediction of T- and H-phase Two-dimensional transition-metal carbides/nitrides and their semiconducting–metallic phase transition, *ChemPhysChem* **18**, 1897 (2017).
- [35] S. Wang, B. Li, L. Li, Z. Tian, Q. Zhang, L. Chen, and X. C. Zeng, Highly efficient N<sub>2</sub> fixation catalysts: Transition-metal carbides M<sub>2</sub>C (MXenes), *Nanoscale* **12**, 538 (2020).
- [36] B. Akgenc, New predicted two-dimensional MXenes and their structural, electronic and lattice dynamical properties, *Solid State Commun.* **303–304**, 113739 (2019).
- [37] R. Ma, G. Lin, Y. Zhou, Q. Liu, T. Zhang, G. Shan, M. Yang, and J. Wang, A review of oxygen reduction mechanisms for metal-free carbon-based electrocatalysts, *npj Comput. Mater.* **5**, 78 (2019).
- [38] V. Viswanathan, H. A. Hansen, J. Rossmeisl, and J. K. Nørskov, Universality in oxygen reduction electrocatalysis on metal surfaces, *ACS Catal.* **2**, 1654 (2012).
- [39] A. Kulkarni, S. Siahrostami, A. Patel, and J. K. Nørskov, Understanding catalytic activity trends in the oxygen reduction reaction, *Chem. Rev.* **118**, 2302 (2018).
- [40] I. C. Man, H.-Y. Su, F. Calle-Vallejo, H. A. Hansen, J. I. Martínez, N. G. Inoglu, J. Kitchin, T. F. Jaramillo, J. K. Nørskov, and J. Rossmeisl, Universality in oxygen evolution electrocatalysis on oxide surfaces, *ChemCatChem* **3**, 1159 (2011).
- [41] J. Rossmeisl, Z. W. Qu, H. Zhu, G. J. Kroes, and J. K. Nørskov, Electrolysis of water on oxide surfaces, *J. Electroanal. Chem.* **607**, 83 (2007).
- [42] NIST Chemistry WebBook, <https://webbook.nist.gov/chemistry/>.
- [43] J. Greeley, I. E. L. Stephens, A. S. Bondarenko, T. P. Johansson, H. A. Hansen, T. F. Jaramillo, J. Rossmeisl, I. Chorkendorff, and J. K. Nørskov, Alloys of platinum and early transition metals as oxygen reduction electrocatalysts, *Nat. Chem.* **1**, 552 (2009).
- [44] N. Govind, M. Petersen, G. Fitzgerald, D. King-Smith, and J. Andzelm, A generalized synchronous transit method for transition state location, *Comput. Mater. Sci.* **28**, 250 (2003).
- [45] E. Fako, A. S. Dobrota, I. A. Pašti, N. López, S. V. Mentus, and N. V. Skorodumova, Lattice mismatch as the descriptor of segregation, stability and reactivity of supported thin catalyst films, *Phys. Chem. Chem. Phys.* **20**, 1524 (2018).
- [46] S. Zhou, X. Yang, W. Pei, N. Liu, and J. Zhao, Heterostructures of MXenes and N-doped graphene as highly active bifunctional electrocatalysts, *Nanoscale* **10**, 10876 (2018).
- [47] C.-Y. Liu and E. Y. Li, Termination effects of Pt/v-Ti<sub>n+1</sub>C<sub>n</sub>T<sub>2</sub> MXene surfaces for oxygen reduction reaction catalysis, *ACS Appl. Mater. Interfaces* **11**, 1638 (2019).
- [48] X. Xie, S. Chen, W. Ding, Y. Nie, and Z. Wei, An extraordinarily stable catalyst: Pt NPs supported on two-dimensional Ti<sub>3</sub>C<sub>2</sub>X<sub>2</sub> (X=OH, F) nanosheets for oxygen reduction reaction, *Chem. Commun.* **49**, 10112 (2013).
- [49] Z. Duan and G. Wang, A first principles study of oxygen reduction reaction on a Pt(111) surface modified by a subsurface transition metal M (M=Ni, Co, or Fe), *Phys. Chem. Chem. Phys.* **13**, 20178 (2011).
- [50] P. Sabatier, Hydrogénations et déshydrogénations par catalyse, *Ber. Dtsch. Chem. Ges.* **44**, 1984 (1911).
- [51] C. Cheng, X. Zhang, and Z. Yang, Low-temperature preferential oxidation of CO over Ag monolayer decorated Mo<sub>2</sub>C (MXene) for purifying H<sub>2</sub>, *J. Phys.: Condens. Matter* **31**, 215201 (2019).
- [52] C. Xu, X. Zhang, and Z. Yang, Efficient metal overlayer catalysts on the Nb<sub>2</sub>C monolayer for CO oxidation from first-principles screening, *J. Phys.: Condens. Matter* **32**, 175201 (2020).
- [53] Z. W. Seh, J. Kibsgaard, C. F. Dickens, I. Chorkendorff, J. K. Nørskov, and T. F. Jaramillo, Combining theory and experiment in electrocatalysis: Insights into materials design, *Science* **355**, eaad4998 (2017).
- [54] Y. Lee, J. Suntivich, K. J. May, E. E. Perry, and Y. Shao-Horn, Synthesis and activities of rutile IrO<sub>2</sub> and RuO<sub>2</sub> nanoparticles for oxygen evolution in acid and alkaline solutions, *J. Phys. Chem. Lett.* **3**, 399 (2012).
- [55] X.-R. Wang, J.-Y. Liu, Z.-W. Liu, W.-C. Wang, J. Luo, X.-P. Han, X.-W. Du, S.-Z. Qiao, and J. Yang, Identifying the Key role of pyridinic-N–Co bonding in synergistic electrocatalysis for reversible ORR/OER, *Adv. Mater.* **30**, 1800005 (2018).
- [56] Z. Wu, H. Wang, P. Xiong, G. Li, T. Qiu, W.-B. Gong, F. Zhao, C. Li, Q. Li, G. Wang, et al., Molecularly thin nitride sheets stabilized by titanium carbide as efficient bifunctional electrocatalysts for fiber-shaped rechargeable zinc-Air batteries, *Nano Lett.* **20**, 2892 (2020).
- [57] D. Kan, D. Wang, X. Zhang, R. Lian, J. Xu, G. Chen, and Y. Wei, Rational design of bifunctional ORR/OER catalysts based on Pt/Pd-doped Nb<sub>2</sub>CT<sub>2</sub> MXene by first-principles calculations, *J. Mater. Chem. A* **8**, 3097 (2020).
- [58] H. Xu, D. Cheng, D. Cao, and X. C. Zeng, A universal principle for a rational design of single-atom electrocatalysts, *Nat. Catal.* **1**, 339 (2018).